PAPER

Method for the Three-Dimensional Imaging of a Moving Target Using an Ultra-Wideband Radar with a Small Number of Antennas

Takuya SAKAMOTO[†a)], **Yuji MATSUKI**[†], ***Members***, ***and*** **Toru SATO**[†], ***Fellow***

SUMMARY Ultra wideband (UWB) radar is considered a promising technology to complement existing camera-based surveillance systems because, unlike cameras, it provides excellent range resolution. Many of the UWB radar imaging algorithms are based on large-scale antenna arrays that are not necessarily practical because of their complexity and high cost. To resolve this issue, we previously developed a two-dimensional radar imaging algorithm that estimates unknown target shapes and motion using only three antennas. In this paper, we extend this method to obtain three-dimensional images by estimating three-dimensional motions from the outputs of five antennas. Numerical simulations confirm that the proposed method can estimate accurately the target shape under various conditions.
key words: *ultra wideband radar, moving target, radar imaging, spheroid, three-dimensional*

1. Introduction

Ultra wideband (UWB) radar is a promising core technology for next-generation surveillance systems because it has high range-resolution and so can complement the high horizontal-resolution provided by conventional camera-based systems. In addition, radar can obtain the shape of the human body without the associated surface textures, thus avoiding privacy concerns caused by cameras used in private places [1]. Although a variety of imaging algorithms have been proposed for UWB radars, most of the conventional imaging methods are based on large-scale antenna arrays [2]–[7], which inevitably makes them too costly to implement in commercial surveillance systems. Some studies assume mechanical scanning antennas instead of array antennas [8], [9], which requires a long time to complete a measurement, making it difficult to realize the real-time operation required for surveillance systems.

One solution to this problem was presented by Lin and Ling [10], [11] who proposed a four-antenna-based radar imaging method using the micro-Doppler, employing different Doppler shifts for multiple parts of the human body. Although this method can obtain images using a small number of antennas, the resulting image is only a vague silhouette of the target, which does not give detailed three-dimensional information. Another solution was presented by Fujita et al. [12] for indoor targets. This method employs multi-path echoes from walls and assumes imaginary mirror images of antennas to obtain high-resolution images with a small number of antennas. This method requires accurate information about the multi-path environments, which is not always practical in actual applications.

To solve the problem and realize a simpler low-cost radar system, we have developed a UWB radar imaging method [13]–[15] that exploits the motion of targets, for instance the human body and a walking motion, rather than requiring a large antenna array setup. This imaging method [15] uses only three antennas, but is still capable of estimating two-dimensional motion and the shape of targets. However, it is necessary to obtain three-dimensional, rather than two-dimensional, images for many surveillance applications.

This paper extends the conventional two-dimensional imaging method to estimate three-dimensional target motions and shapes. In the conventional two-dimensional imaging method, a circular model with three parameters was used to approximate the local shape of a target. In our proposed three-dimensional method, we use a spheroidal model based on five parameters. Therefore, we assume a radar system with five antennas to solve these five unknowns using the received signal data. The performance of the proposed method is investigated using numerical simulations. We also calculate the imaging accuracy of the proposed method under various conditions, by changing the shape and motion of the target, the effect of noise, and the antenna intervals, to clarify the performance parameters of the method.

2. System Model

Figure 1 shows a schematic of the proposed radar system, in which five antennas are installed on a wall of a passage way. For simplicity, the target is modeled as a smooth, convex object with a sharp boundary profile. A reference point on the target surface is chosen to represent the target position $\boldsymbol{X}_{\mathrm{m}}(t) = (X_{\mathrm{m}}(t), Y_{\mathrm{m}}(t), Z_{\mathrm{m}}(t))$ at time t. The target translational motion $\boldsymbol{X}_{\mathrm{m}}$ is assumed to be arbitrary and unknown. The five antennas are in a cruciform arrangement in the $x-z$ plane with separation Δx, i.e. the five antenna coordinates for #1, #2, $\cdots$, #5 are $(-\Delta x, 0, 0)$, $(0, 0, 0)$, $(\Delta x, 0, 0)$, $(0, 0, -\Delta x)$, and $(0, 0, \Delta x)$. The assumed layout of the antennas and the coordinate system are illustrated in Fig. 2. Each antenna is assumed to be omni-directional and connected to a transmitter and receiver with switches, functioning as five independent mono-static radar systems. Transmitted signals are modulated so they do

Manuscript received May 13, 2011.
Manuscript revised October 13, 2011.
[†]The authors are with the Department of Communications and Computer Engineering, Graduate School of Informatics, Kyoto University, Kyoto-shi, 606-8501 Japan.
a) E-mail: t-sakamo@i.kyoto-u.ac.jp
DOI: 10.1587/transcom.E95.B.972

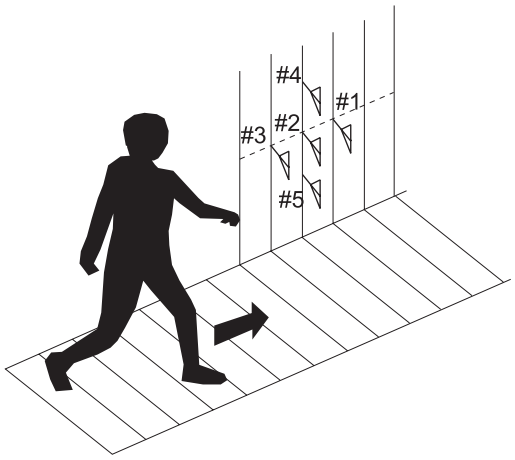

Fig. 1 Proposed radar system for surveillance systems.

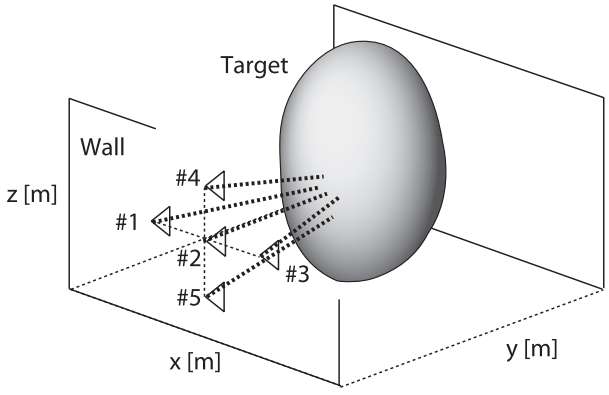

Fig. 2 Schematic of radar system model.

not interfere with other signals. The pulse repetition period is set to Δt. The distance between the i-th antenna and the corresponding scattering center at time t is defined as $R_i(t)$ for $i = 1, 2, \cdots, 5$. The purpose of the proposed method in the paper is to estimate the target motion $\boldsymbol{X}_{\mathrm{m}}(t)$ and shape using these five range data.

3. Conventional Two-Dimensional Imaging Method

Our previous work [15] proposed a two-dimensional imaging method. The method uses three antennas #1, #2, and #3 of the five shown in Fig. 2 to estimate the two-dimensional cross-section shape of a target in translational motion. The motion is assumed to be two-dimensional, which means the z-component is fixed to zero $Z_{\mathrm{m}}(t) = 0$. The method approximates the local shape of a target with a circle, termed a curvature circle. A curvature circle has three parameters, a curvature center $\boldsymbol{c}(t) = (c_x(t), c_y(t))$ and a curvature radius $a(t)$. These parameters are determined using the data $R_1(t), R_2(t)$ and $R_3(t)$ solving the following simultaneous equations.

$$\begin{cases} R_1(t) &= \sqrt{(c_x(t) + \Delta x)^2 + (c_y(t))^2} - a(t) \\ R_2(t) &= \sqrt{(c_x(t))^2 + (c_y(t))^2} - a(t) \\ R_3(t) &= \sqrt{(c_x(t) - \Delta x)^2 + (c_y(t))^2} - a(t) \end{cases}$$

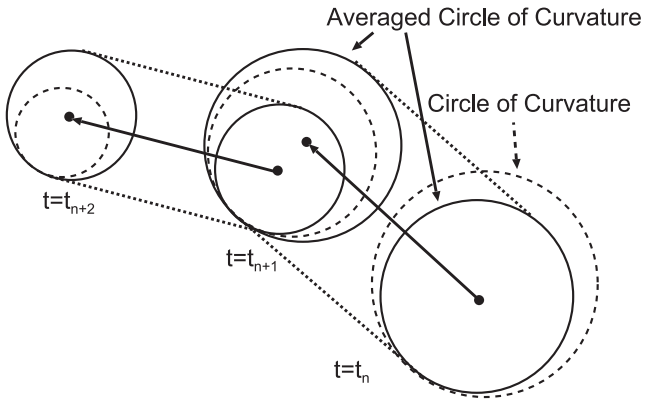

Fig. 3 A schematic of the averaging circles of curvature in the two-dimensional imaging method.

Note that the motion $\boldsymbol{c}(t)$ contains not only the target motion $\boldsymbol{X}_{\mathrm{m}}(t)$ but also the effect of the relative motion of a scattering center along the target surface. Therefore, $\boldsymbol{c}(t)$ cannot be used directly as an estimate of the target motion.

To overcome this difficulty, the proposed method calculates an average radius of curvature using adjacent radii $a(t_n)$ and $a(t_{n+1})$ as $\bar{a}(t_{n+\frac{1}{2}}) = (a(t_n) + a(t_{n+1}))/2$. Then, $\boldsymbol{c}(t_n)$ and $\boldsymbol{c}(t_{n+1})$ are recalculated as $\bar{\boldsymbol{c}}(t_n)$ and $\bar{\boldsymbol{c}}(t_{n+1})$ using least-mean-square criteria, subject to the condition that the radius of curvature is equal to $\bar{a}(t_{n+\frac{1}{2}})$ for both $t = t_n$ and $t = t_{n+1}$. An instantaneous velocity vector $\boldsymbol{v}_{n+\frac{1}{2}}$ is defined as

$$\boldsymbol{v}_{n+\frac{1}{2}} = (\bar{\boldsymbol{c}}(t_{n+1}) - \bar{\boldsymbol{c}}(t_n))/\Delta t. \tag{1}$$

This operation enables the separation of the target motion $\boldsymbol{X}_{\mathrm{m}}(t)$ from the relative motion of the scattering center [15]. Figure 3 shows a schematic of this procedure, where three circles of curvature for successive time shots $t = t_n, t_{n+1}, t_{n+2}$ have been drawn with dashed lines. The averaged circles of curvature using successive pairs $t = t_n, t_{n+1}$ and t_{n+1}, t_{n+2} are depicted with solid lines.

Finally, we integrate the instantaneous velocity vector to obtain an estimate of the target location $\bar{\boldsymbol{X}}(t_N) = \sum \boldsymbol{v}_{n+\frac{1}{2}} \Delta t + \boldsymbol{X}(0)$. Note that the initial value $\boldsymbol{X}(0)$ does not have any effect on the imaging results because it affects only the location of the estimated image. By compensating for this estimated target motion $\bar{\boldsymbol{X}}(t)$, the estimated scattering centers are transferred to the initial position at $t = 0$ to form an image.

4. Proposed Three-Dimensional Imaging Algorithm

We present an extended version of the above method applicable to three-dimensional cases. This method approximates the local shape of the target with a spheroid instead of a circle. A spheroid is a surface that is obtained by rotating an ellipse about its principal axis. We use all five antennas to estimate the five parameters of a spheroid expressed using a center $\boldsymbol{c}(t) = (c_x(t), c_y(t), c_z(t))$, and the respective horizontal and vertical radii $a(t)$ and $b(t)$ as

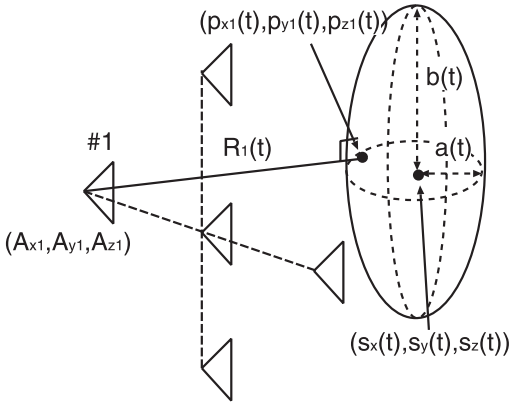

Fig. 4 Relationship between parameters for deriving equations.

$$\frac{(x-c_x(t))^2}{a(t)^2}+\frac{(y-c_y(t))^2}{a(t)^2}+\frac{(z-c_z(t))^2}{b(t)^2}=1. \tag{2}$$

Using the five ranging data $Ri(t)$ $(i = 1, 2, \cdots, 5)$ from the five antennas, these five spheroid parameters $(c_x(t), c_y(t), c_z(t), a(t), b(t))$ are determined as follows. We define $\boldsymbol{p}_i(t) = (p_{x,i}(t), p_{y,i}(t), p_{z,i}(t))$ as the scattering center position at time t as for the antenna #i located at $(A_{x,i}, A_{y,i}, A_{z,i})$. Figure 4 illustrates the relationship of these parameters for antenna #1 as an example.

First, the scattering center $(p_{x,i}(t), p_{y,i}(t), p_{z,i}(t))$ is located on the spheroidal model as in Eq. (2) replacing x, y, and z with $p_{x,i}(t), p_{y,i}(t), p_{z,i}(t)$. Next, the antenna position $(A_{x,i}, A_{y,i}, A_{z,i})$ is on the normal line as

$$\begin{pmatrix}A_{x,i}\\A_{y,i}\\A_{z,i}\end{pmatrix}=\begin{pmatrix}p_{x,i}(t)\\p_{y,i}(t)\\p_{z,i}(t)\end{pmatrix}+t_i\begin{pmatrix}\frac{2(p_{x,i}(t)-c_x(t))}{a(t)^2}\\\frac{2(p_{y,i}(t)-c_y(t))}{a(t)^2}\\\frac{2(p_{z,i}(t)-c_z(t))}{b(t)^2}\end{pmatrix}, \tag{3}$$

where t_i is a parameter proportional to the echo delay. Finally, for the distance between the antenna and the scattering center $R_i(t)$, the following equation holds:

$$\begin{aligned}(A_{x,i}-p_{x,i}(t))^2 &+ (A_{y,i}-p_{y,i}(t))^2\\ &+ (A_{z,i}-p_{z,i}(t))^2 = R_i(t)^2.\end{aligned} \tag{4}$$

These simultaneous equations Eqs. (2), (3) and (4) are derived for the five antennas $(i = 1, 2, \cdots, 5)$ and solved for $(c_x(t), c_y(t), c_z(t), a(t), b(t))$ using Brent's method [16].

Although translational motion $(c_x(t), c_y(t), c_z(t))$ can be estimated approximately using these parameters, it is not identical to the center position $\boldsymbol{c}(t)$ for the same reason as in the two-dimensional case. The proposed method calculates averaged horizontal and vertical radii using two adjacent samples as $\bar{a}_{n+\frac{1}{2}} = (a(t_n) + a(t_{n+1}))/2$ and $\bar{b}_{n+\frac{1}{2}} = (b(t_n) + b(t_{n+1}))/2$. These averaged radii are then used for recalculating the center positions $\bar{\boldsymbol{c}}(t_n)$ and $\bar{\boldsymbol{c}}(t_{n+1})$ using the estimated scattering center positions $\boldsymbol{p}_i(t)(i = 1, 2, \ldots, 5)$. The center positions $\bar{\boldsymbol{c}}(t_n)$ and $\bar{\boldsymbol{c}}(t_{n+1})$ are optimized while the other two parameters are fixed as $a = \bar{a}_{n+\frac{1}{2}}$ and $b = \bar{b}_{n+\frac{1}{2}}$ to minimize the distance between the spheroid surface and the scattering centers $\boldsymbol{p}_i(t_n)$ and $\boldsymbol{p}_i(t_{n+1})(i = 1, 2, \ldots, 5)$, respectively. Finally, these center positions $\bar{\boldsymbol{c}}(t_n)$ and $\bar{\boldsymbol{c}}(t_{n+1})$ are used to calculate an instantaneous velocity vector $\boldsymbol{v}_{n+\frac{1}{2}} = (\bar{\boldsymbol{c}}(t_{n+1}) - \bar{\boldsymbol{c}}(t_n))/\Delta t$ exactly like the two-dimensional case.

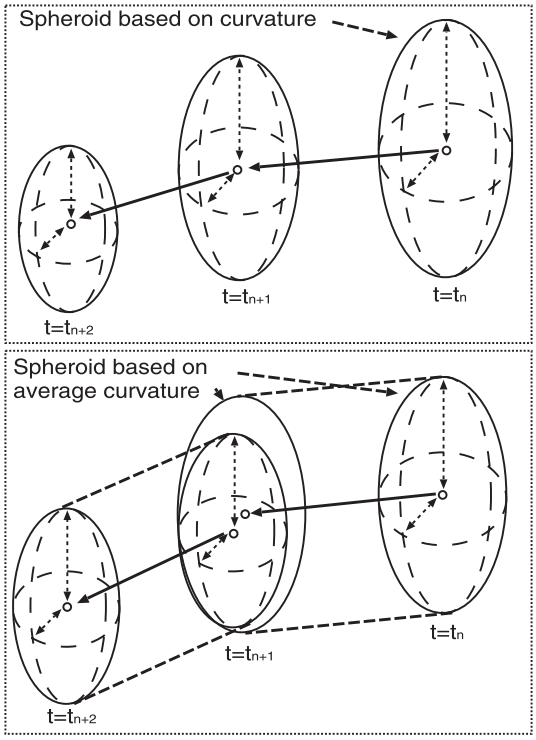

Fig. 5 Estimated velocity vectors using the motion estimation methods with/without averaging of the radii.

Figure 5 shows the difference between the methods with/without the averaging process applied to the horizontal and vertical radii. The averaging of the radii was introduced in our proposed method because it can eliminate the motion of scattering centers from the motion of the spheroidal model. This averaging process displaces the velocity vectors as shown for the spheroid at $t = t_{n+1}$ in the lower image in Fig. 5. Next, these estimated velocity vectors are summed to obtain the target motion as

$$\bar{\boldsymbol{X}}_{\mathrm{m}}(t_N) = \sum_{n=1}^{N-1} \boldsymbol{v}_{n+\frac{1}{2}}\Delta t + \boldsymbol{X}_{\mathrm{m}}(0). \tag{5}$$

Lastly, the final image is obtained by translating the scattering center positions $\boldsymbol{p}_i(t)(i = 1, 2, \ldots, 5)$, compensating for the estimated target motion.

After obtaining the image, we apply an artifact suppression method. This method eliminates the point $\boldsymbol{x}_i$ that satisfies

$$\min_j |\boldsymbol{x}_i - \boldsymbol{x}_j| > \Delta d \quad (i \neq j). \tag{6}$$

This process is based on the assumption that most of the artifacts are isolated from other points. Thus, a point separated from other points with minimum Δd-proximity can be eliminated. The value Δd is empirically determined.

5. Application of the Proposed Method to a Distorted Ellipsoidal Target

We investigate the performance of the proposed method by applying it to an asymmetrically distorted ellipsoidal target. Figure 6 displays the assumed target shape and motion. The target shape is expressed as

$$\begin{pmatrix} x(\theta,\phi) \\ y(\theta,\phi) \\ z(\theta,\phi) \end{pmatrix} = \begin{pmatrix} A(1+\delta\cos\theta)\cos\theta\sin\phi \\ B(1+\delta\cos(\theta+\pi/4))\sin\theta\sin\phi \\ C\cos\phi \end{pmatrix}, \quad (7)$$

where we set $A = 0.15$ m, $B = 0.25$ m, $C = 0.85$ m, $\delta = 0.5$, $0 \le \theta \le 2\pi$, and $0 \le \phi \le \pi$. These parameters have been chosen for application to human body imaging. The image at the upper right section in Fig. 6 is the horizontal cross section of the target. The target motion is expressed as $\boldsymbol{X}_{\rm m}(t) = (x_0 + v_x t, y_0 + y_f \sin(\omega t + \chi_0), z_0 \sin(\omega t + \chi_0))$, wehre $x_0 = 2.0$ m, $v_x = -1.0$ m/s, $y_0 = 1.0$ m, $y_f = 0.25$ m, $z_0 = 0.25$ m, $\omega = \pi/4$ rad/s, and $\chi_0 = \pi/2$ rad. We also assume the antenna intervals $\Delta x = 0.5$ m, sampling intervals $\Delta t = 4$ ms and measurement time of $0\,\text{s} \le t \le 4\,\text{s}$. A noiseless environment is assumed in this section. The parameter for artifact suppression is set at $\Delta d = 5.0$ mm, and throughout this paper, Δd is fixed at this value.

The proposed method optimizes the spheroidal numerical model using the received data $R_i(t)(i = 1, 2, \ldots, 5)$, some snapshots of which are shown in Fig. 7. In the figure, the solid and dashed lines show the actual target shapes and the calculated ellipsoidal model shapes. Figure 8 provides the topview of the same image in Fig. 7. Each of these model shapes are estimated based on the local shape of each target. Therefore, the calculated model shapes are not necessarily identical to the actual target shapes as seen in the figure. The white dots in the figure are the scattering center points $(p_{x,i}(t), p_{y,i}(t), p_{z,i}(t))$ estimated using the proposed method. The center position of the estimated ellipsoidal model moves along the curved dashed line 1 in Fig. 9. In our proposed method, the estimation root-mean-square (RMS) error of the target motion is 162.8 mm without the averaging process.

We then show the target motion estimated using the proposed method with the radii averaging process as the dashed line 2 in the figure. By introducing the averaging process, the motion estimation accuracy is improved from 162.8 mm to 21.5 mm. Finally, the estimated scattering centers are translated to obtain the target shape at $t = 0$ by compensating for the estimated translated motion as in Fig. 10. The imaging RMS error is 8.2 mm using our

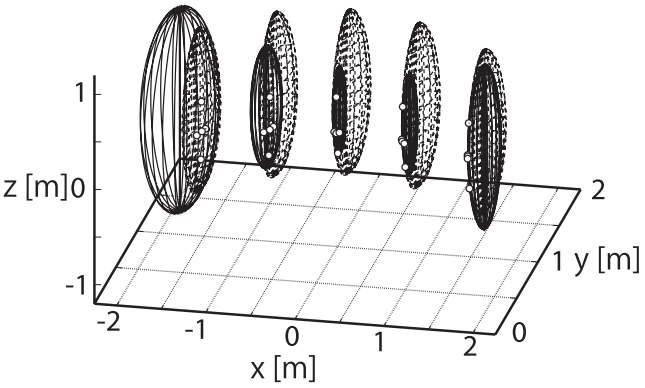

Fig. 7 Actual target shapes (dashed lines) and estimated ellipsoidal model shapes (solid lines) for an asymmetrical target.

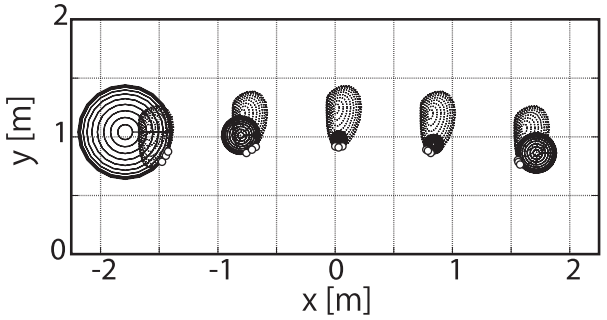

Fig. 8 Topview of Fig. 7.

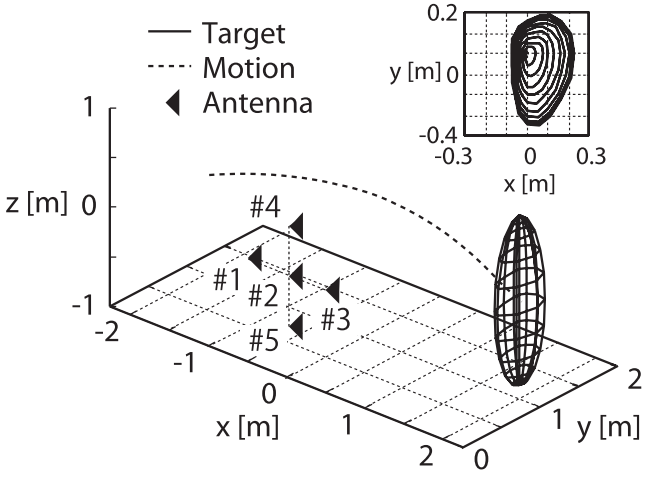

Fig. 6 Asymmetrically distorted ellipsoidal target shape and motion.

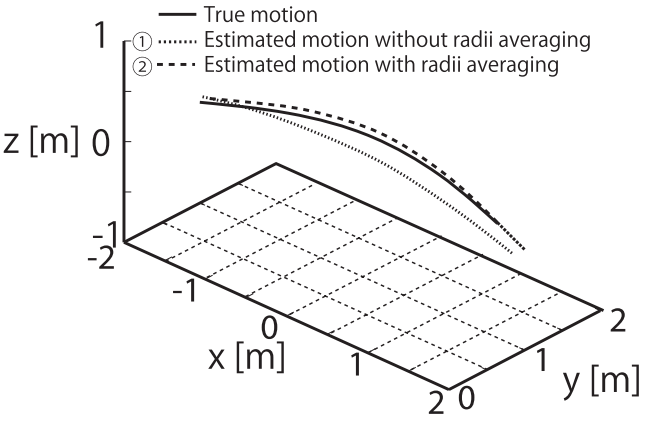

Fig. 9 Estimated target motion using the proposed method for an asymmetrical target.

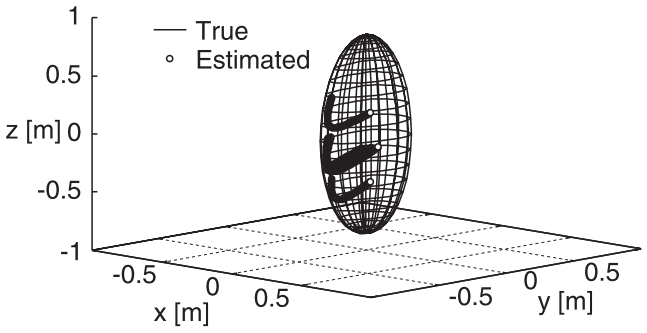

Fig. 10 Estimated image using the proposed method for an asymmetrical target.

proposed method. This result indicates that the proposed method can be applied to a general distorted target although the numerical model is a symmetrical spheroid.

6. Performance of the Proposed Method under Various Conditions

6.1 Imaging Accuracy for Various Target Shapes

We now calculate the imaging accuracy of the proposed method for various values of the x-axis-radius A from 0.15 m to 0.5 m. This parameter range is selected based on the size of an actual human body. Other parameters remain fixed to the same values as in the previous section. Figure 11 shows the relationship between A and the imaging RMS errors of the proposed method. It is seen that the RMS error has a minimum value at $A = 0.25$ m, satisfying $A = B$ that corresponds to a spheroid. Since the proposed method assumes a spheroidal model, this specific case corresponds to the ideal case, where the model is identical to the actual target shape. For target shapes with $A \neq B$, the RMS error becomes larger but is less than 11.5 mm for the assumed parameter range. This means that the proposed method can be applied to wide range of target shapes, with an accuracy high enough for the applications assumed in the paper.

6.2 Imaging Accuracy and Target Motion

Next, we investigate the imaging accuracy of the proposed method for various target motions. We assume the target shape is an ellipsoid with $A = 0.15$ m, $B = 0.25$ m and $C = 0.85$ m. The target motion is $(X_{\mathrm{m}}(t), Y_{\mathrm{m}}(t), Z_{\mathrm{m}}(t)) = (x_0 + v_x t, y_0, z_0 \sin(\omega t + \chi_0))$, where $x_0 = 2.0$ m, $v_x = -1.0$ m/s, $y_0 = 1.0$ m, $\omega = \pi/2$ rad/s, and $\chi_0 = 0$ rad are assumed. We vary the parameter z_0 from 0 m to 0.5 m, which corresponds to a vertical springing motion in normal human gait.

Figure 12 shows the relationship between the RMS error of the proposed method and the vertical amplitude z_0. The parameter $z_0 = 0$ m corresponds to a uniform motion. The minimum RMS error is achieved for the uniform motion with $z_0 = 0$, while the error becomes larger for other cases. The RMS error values for $z_0 = 0$ m and $z_0 = 0.5$ m are 5.4 mm and 9.2 mm. It can be said that the accuracy

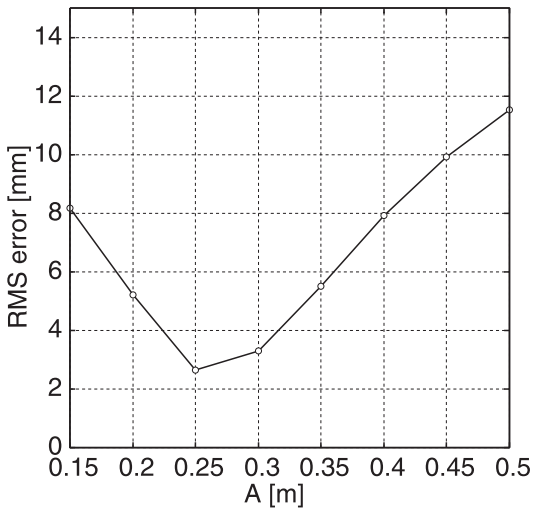

Fig. 11 Relationship between imaging accuracy and the x-axis radius of the target.

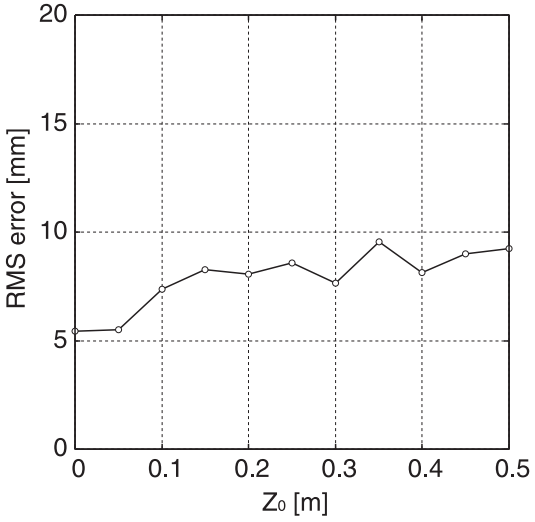

Fig. 12 Relationship between imaging accuracy and vertical target motion parameter z_0.

is not very sensitive to the target motion, which indicates the robustness of the proposed method for various motions. This is because the proposed method estimates the spheroid optimized for range data at each time step. Therefore, the target motion itself does not affect the estimation accuracy.

6.3 Performance Evaluation in Noisy Environment

We now investigate the imaging accuracy of the proposed method in noisy environments. The target shape is assumed to be as in the previous section. The target motion is assumed to be uniform $(X_{\mathrm{m}}(t), Y_{\mathrm{m}}(t), Z_{\mathrm{m}}(t)) = (x_0 + v_x t, y_0, z_0)$, where $x_0 = 2.0$ m, $v_x = -1.0$ m/s, $y_0 = 1.0$ m, and $z_0 = 1.0$ m. White Gaussian random components are added to each of the range data $R_i(t)(i = 1, 2, \ldots, 5)$ to simulate a noisy environment. The relationship between the squared errors in the range data and the received signal power is lin-

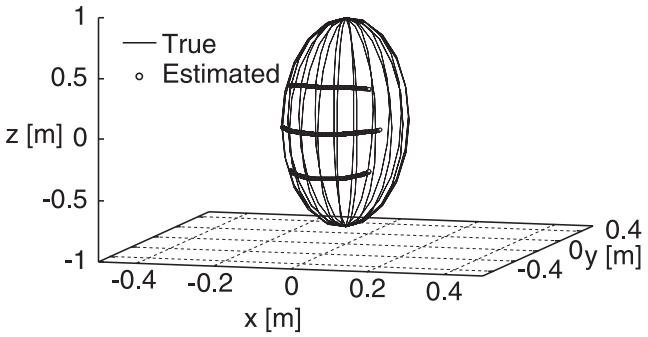

Fig. 13 Estimated target image in a noisy environment with the lowest S/N = 15 dB.

ear for large signal-to-noise ratio (S/N) as in [17]. The S/N is defined as the signal and noise power after applying the matched filter. The signal power is calculated based on a free space model, in which the target cross-section dependency is not taken into account. We assume the lowest S/N to be 15 dB, for which the range data $R_i(t)$ has its maximum value. As in the reference [17], ranging accuracy significantly deteriorated for S/N < 15 dB. Therefore, this assumption of S/N can be considered the worst case scenario when ranging is performed appropriately.

Figure 13 shows the estimated image under these conditions. The RMS error of the image is 6.7 mm, which demonstrates that the proposed method is capable of estimating target shape and motion even in noisy environments. Further study is needed to clarify the necessary system requirements and minimum S/N for which the proposed method can be applied.

6.4 Imaging Accuracy and Antenna Intervals

Finally, we investigate the imaging accuracy of the proposed method for various antenna intervals. The assumed target shape and motion are the same as in the previous section. Figure 14 shows the RMS error of the imaging using the proposed method for various antenna intervals $0.1\,\mathrm{m} \le \Delta x \le 1.0\,\mathrm{m}$ under a noiseless environment.

It is clear that as the antenna interval increases, the imaging error becomes larger mainly for the following reason. For a large antenna interval, the scattering center points are well separated from one another. Because the proposed method approximates the local shape of a target by model fitting, the separated scattering centers do not represent a local shape, making it difficult to apply this approach. As a result, imaging accuracy deteriorates for large Δx.

Figure 15 shows the RMS error vs. the antenna interval for a noisy case with a minimum S/N=15 dB, the same S/N as in the previous section. This figure shows the accuracy is severely degraded for an antenna interval shorter than 0.5 m. Note that in a noisy environment, a small antenna interval increases imaging error sensitivity to background noise. Therefore, an optimum antenna interval should be determined based on the S/N ratio of the data.

Figure 16 shows the S/N and the antenna intervals Δx

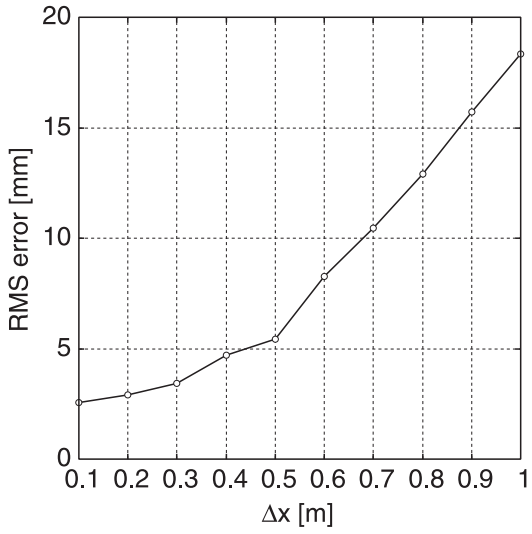

Fig. 14 Relationship between imaging accuracy and antenna interval Δx for noiseless case.

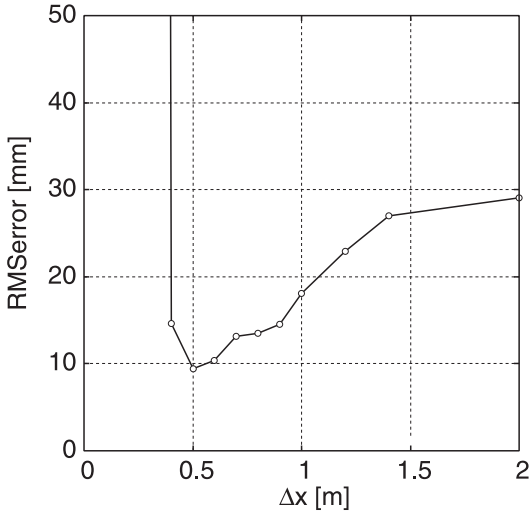

Fig. 15 Relationship between imaging accuracy and antenna interval Δx for noisy data with the minimum S/N=15 dB.

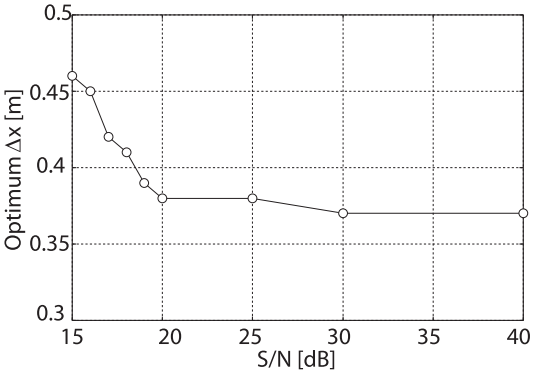

Fig. 16 Relationship between S/N and optimum antenna intervals.

optimized to minimize the imaging RMS error. Depending on the S/N, the optimum antenna intervals change but in a limited range. In particular, the optimum antenna intervals are almost constant around 0.37 m for S/N > 20 dB.

Note that the error values shown above are dependent on the target shape, which makes it difficult to evaluate the imaging error analytically because the target shape can be arbitrary. More realistic computer simulations and/or experimental studies are needed to examine its performance, which is an important task for the future.

7. Discussion

The simulations in this paper have dealt with a relatively simple scenario. In actual environments, there are some other technical issues to be addressed as follows:

- Multiple Interfering Echoes:
  Multiple overlapping echoes must be separated to estimate the range values. A typical approach is the CLEAN algorithm [18] for convolving them sequentially. Another approach is the extended Capon method [19] to separate multiple waveforms using a super-resolution technique.
- Waveform Distortion:
  Scattering waveforms depend on the local shape of the target. This generates bias error to ranging estimation. To eliminate this bias error, the spectrum shift correction method [20] can be used. This method detects the spectrum shift caused by the waveform distortion, and systematically corrects the ranging error.
- Other Factors:
  Shadowing effect, multipath echoes, and antenna coupling have to be addressed to implement the proposed system in practice. It is an important future task to establish optimized system parameters taking into account these factors.

8. Conclusions

In this study, we proposed an imaging method for simple UWB radar systems with five antennas; it uses the motion of the target. This method estimates three-dimensional target motion, and then obtains three-dimensional target images by compensating for the motion. This approach is an extension of the conventional two-dimensional imaging method for three-antenna radar system. The proposed method assumes a spheroidal model to approximate the local shape of the target. The performance of the proposed method has been verified using numerical simulations. The imaging accuracy was also quantitatively evaluated for various models. Simulation results showed that the proposed method can accurately estimate three-dimensional target shapes in a number of scenarios.

References

[1] A. Senior, S. Pankanti, A. Hampapur, L. Brown, Y.-L. Tian, A. Ekin, J. Connell, Chiao Fe Shu, and M. Lu, "Enabling video privacy through computer vision," IEEE Security & Privacy, vol.3, no.3, pp.50–57, May–June 2005.

[2] C.J. Leuschen and R.G. Plumb, "A matched-filter-based reverse-time migration algorithm for ground-penetrating radar data," IEEE Trans. Geosci. Remote Sens., vol.39, no.5, pp.929–936, May 2001.

[3] A.G. Yarovoy, T.G. Savelyev, P.J. Aubry, P.E. Lys, and L.P. Ligthart, "UWB array-based sensor for near-field imaging," IEEE Trans. Microw. Theory Tech., vol.55, no.6, pp.1288–1295, June 2007.

[4] S. Masuyama and A. Hirose, "Walled LTSA array for rapid, high spatial resolution, and phase-sensitive imaging to visualize plastic landmines," IEEE Trans. Geosci. Remote Sens., vol.45, no.8, pp.2536–2543, Aug. 2007.

[5] M. Dehmollaian and K. Sarabandi, "Refocusing through building walls using synthetic aperture radar," IEEE Trans. Geosci. Remote Sens., vol.46, no.6, pp.1589–1599, June 2008.

[6] Y. Yang and A.E. Fathy, "Development and implementation of a real-time see-through-wall radar system based on FPGA," IEEE Trans. Geosci. Remote Sens., vol.47, no.5, pp.1270–1280, May 2009.

[7] X. Zhuge, A.G. Yarovoy, T. Savelyev, and L. Ligthart, "Modified Kirchhoff migration for UWB MIMO array-based radar imaging," IEEE Trans. Geosci. Remote Sens., vol.48, no.6, pp.2692–2703, June 2010.

[8] T. Sakamoto and T. Sato, "A target shape estimation algorithm for pulse radar systems based on boundary scattering transform," IEICE Trans. Commun., vol.E87-B, no.5, pp.1357–1365, May 2004.

[9] T. Sakamoto, "A fast algorithm for 3-dimensional imaging with UWB pulse radar systems," IEICE Trans. Commun., vol.E90-B, no.3, pp.636–644, March 2007.

[10] A. Lin and H. Ling, "Frontal imaging of human using three-element Doppler and direction-of-arrival radar," Electron. Lett., vol.42, no.11, pp.660–661, 2006.

[11] A. Lin and H. Ling, "Three-dimensional tracking of humans using very low-complexity radar," Electron. Lett., vol.42, no.18, pp.1062–1063, 2006.

[12] S. Fujita, T. Sakamoto, and T. Sato, "2-dimensional accurate imaging with UWB radar using indoor multipath echoes for a target in shadow regions," IEICE Trans. Commun., vol.E94-B, no.8, pp.2366–2374, Aug. 2011.

[13] T. Sakamoto, Y. Matsuki, and T. Sato, "A novel UWB radar 2-D imaging method with a small number of antennas for targets with arbitrary shapes and motion," Proc. 2009 IEEE International Conference on Ultra-WideBand (ICUWB2009), pp.449–453, Sept. 2009.

[14] Y. Matsuki, T. Sakamoto, and T. Sato, "Study of a method for 2-D imaging of simple-shaped targets with arbitrary motion using UWB radar with a small number of antennas," Proc. 20th International Conference on Applied Electromagnetics and Communications (ICECom 2010), Sept. 2010.

[15] Y. Matsuki, T. Sakamoto, and T. Sato, "An imaging algorithm of a target with arbitrary motion for ultra wide-band radar with a small number of antennas," IEICE Trans. Commun., vol.E94-B, no.3, pp.742–749, March 2011.

[16] R.P. Brent, Algorithms for Minimization without Derivatives, Prentice Hall, 1972.

[17] T. Sakamoto, "A 2-D image stabilization algorithm for UWB pulse radars with fractional boundary scattering transform," IEICE Trans. Commun., vol.E90–B, no.1, pp.131–139, Jan. 2007.

[18] R. Bose, A. Freedman, and B.D. Steinberg, "Sequence CLEAN: A modified deconvolution technique for microwave images of contiguous targets," IEEE Trans. Aerosp. Electron. Syst., vol.38, no.1, pp.89–97, 2002.

[19] S. Kidera, T. Sakamoto, and T. Sato, "Super-resolution UWB radar imaging algorithm based on extended capon with reference signal optimization," IEEE Trans. Antennas Propag., vol.59, no.5, pp.1606–1615, 2011.

[20] S. Kidera, T. Sakamoto, and T. Sato, "High-resolution and real-time

3-D imaging algorithm with envelope of spheres for UWB radars," IEEE Trans. Geosci. Remote Sens., vol.46, no.11, pp.3503–3513, 2008.

Takuya Sakamoto received his B.E. degree from Kyoto University in 2000, and M.I. and Ph.D. degrees from the Graduate School of Informatics, Kyoto University in 2002 and 2005, respectively. He is Assistant Professor in Graduate School of Informatics, Kyoto University. He is also Visiting Associate in Delft University of Technologywith the support of JSPS Postdoctoral Fellowships for Research Abroad. His current research interest is in radar and ultrasonic imaging algorithms. He is a member of the IEEJ and the IEEE.

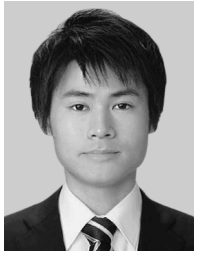

Yuji Matsuki received his B.E. degree from Kyoto University in 2009, and M.I. degree from the Graduate School of Informatics, Kyoto University in 2011. His current research interest is in radar signal processing.

Toru Sato received his B.E., M.E., and Ph.D. degrees in electrical engineering from Kyoto University, Kyoto, Japan in 1976, 1978, and 1982, respectively. He has been with Kyoto University since 1983 and is currently a Professor in the Department of Communications and Computer Engineering, Graduate School of Informatics. His major research interests are system design and signal processing aspects of atmospheric radar, radar remote sensing of the atmosphere, observations of precipitation using radar and satellite signals, radar observation of space debris, and signal processing for subsurface radar signals. Dr. Sato was awarded the Tanakadate Prize in 1986. He is a member of the Institute of Electronics, Information, and Communication Engineers of Japan, the Society of Geomagnetism and Earth, Planetary and Space Sciences, the Japan Society for Aeronautical and Space Sciences, the Institute of Electrical and Electronics Engineers, and the American Meteorological Society.